Spatial Mesh Refinement using Cubic Smoothing Spline Interpolation in Simulation of 2-D Elastic Wave Equation: Forward Modeling of Full-waveform Inversion

Original Research Article

Abstract

Full-waveform inversion (FWI) is a non-destructive health monitoring technique that can be used to identify and quantify the embedded anomalies. The forward modeling of the FWI consists of a simulation of elastic wave equation to generate synthetic data. Thus the accuracy of the FWI method highly depends on the simulation method used in the forward modeling. Simulation of a 3-D seismic survey with small-scale heterogeneities is impossible with the classic finite difference approach even on modern super computers. In this work, we adopted a mesh refinement approach for simulation of the wave equation in the presence of small-scale heterogeneities. This approach uses cubic smoothing spline interpolation for spatial mesh refinement step in solving the wave equation. The simulation results for the 2-D elastic wave equation are presented and compared with the classic finite difference approach.

Keywords: Full-waveform inversion, Elastic wave propagation, Heterogeneities, Cubic smoothing spline interpolation

2010 Mathematics Subject Classification: 53C25; 83C05; 57N16

1 Introduction

Full-waveform inversion (FWI) approach [Sjögreen & Petersson (2014); Tran & McVay (2012); Xu et al. (2012); Lee & Kim (2003); Charara et al. (2000); Ha & Shin (2012)] is a non-destructive testing method that can be used to identify and quantify embedded sinkholes. FWI can determine the properties of the subsurface from seismic data (wavefield data) obtained at receivers, which are placed on the

subsurface. This method offers the potential to produce higher resolution imaging of the subsurface by extracting information contained in the complete waveforms [Tran & McVay (2012)].

The accuracy of the results, and the efficacy of the FWI method, depend on the numerical approaches that were used in simulation of seismic wave propagation. In the FWI method, the forward modeling consists of generating synthetic wavefields. In Ref. Tran & McVay (2012) the synthetic wavefield is generated by solving 2-D elastic wave equations using a classic velocity-stress staggered-grid finite difference scheme [Liu & Sen (2009); Crase (1990); Xia et al. (2004); Di Bartolo et al. (2012)] with a uniform grid. Simulation of elastic wave equations with small-scale heterogeneities can be done with the classic finite difference approach, at small step sizes, with uniform grid. However, simulation of a 3-D seismic survey with small-scale heterogeneities is impossible with the classic finite difference approach, even on modern supercomputers, due to large number of source gatherings and grid points [Kostin et al. (2015)]. Therefore, a mesh refinement approach (or multi-grid method) that can be applied to different regions of domain with different step sizes is needed.

Ref. Kostin et al. (2015) introduced an approach for numerical simulation of wave propagation in media with sub-seismic-scale heterogeneities such as cavities and fractures. Their method is based on local mesh refinement with respect to time and space. The main features of the approach are the use of temporal and spatial refinement on two different surfaces, use of the embedded-stencil technique of grid step with respect to time, and use of the fast Fourier based interpolation to couple variables for spatial mesh refinement.

We adapted the approach introduced in Ref. Kostin et al. (2015) with some modifications. For spatial mesh refinement, Ref. Kostin et al. (2015) used the fast Fourier based interpolation. However, in this work, we modify the technique with cubic smoothing spline interpolation [Hutchinson (1986); De Boor et al. (1978); Cook & Peters (1981); Hou & Andrews (1978)] rather than the finite Fourier interpolation for spatial mesh refinement. By using cubic smoothing spline interpolation, we can achieve better results for wavefield data for the fine grid zone. For the comparison, we simulate a 2-D elastic wave equation with both the modified technique and the technique in Ref. Kostin et al. (2015). The results of both methods are compared with a uniform mesh method. The cubic smoothing spline interpolation method show a significant improvement as compared to instead using the finite Fourier interpolation method.

The rest of the chapter is arranged as follows. Approximated model of 2-D wave equations using classic finite difference approximation with a uniform grid is discussed in Section 2. Section 3 presents the modified local mesh refinement method with cubic spline interpolation. The results for 2-D wave propagation are presented in Section 4.

2 Simulation of 2-D elastic wave equations using a uniform mesh

2.1 2-D wave equation

The FWI technique consists of two stages. The first stage induces forward modeling to generate synthetic wave-fields, and the second stage includes the model updating by considering when the residual between predicted and measured surface velocities are negligible. Forward modeling of FWI develops the solutions of the 2-D elastic wave equations. We simulate wave propagation by solving 2-D elastic wave equations [Appelö & Petersson (2009); Liang-Guo et al. (2000); Kosloff et al. (1984); Woodward (1992)] numerically using Cartesian coordinates.

Let σ_{xx}, σ_{zz}, and σ_{xz} be the components of stress tensor and u, v be the particle velocity components. The spatial directions in the 2D plane are x and z.

Then the equations governing particle velocity in 2-D are

$$\frac{\partial u}{\partial t} = \frac{1}{\rho}\left(\frac{\partial \sigma_{xx}}{\partial x} + \frac{\partial \sigma_{xz}}{\partial z}\right) = f_1(\rho) \tag{2.1}$$

$$\frac{\partial v}{\partial t} = \frac{1}{\rho}\left(\frac{\partial \sigma_{xz}}{\partial x} + \frac{\partial \sigma_{zz}}{\partial z}\right) = f_2(\rho) \tag{2.2}$$

and the equations governing stress-strain tensor are

$$\frac{\partial \sigma_{xx}}{\partial t} = (\lambda + 2\mu)\frac{\partial u}{\partial x} + \lambda\frac{\partial v}{\partial z} = f_3(\lambda, \mu) \tag{2.3}$$

$$\frac{\partial \sigma_{zz}}{\partial t} = \lambda\frac{\partial u}{\partial x} + (\lambda + 2\mu)\frac{\partial v}{\partial z} = f_4(\lambda, \mu) \tag{2.4}$$

$$\frac{\partial \sigma_{xz}}{\partial t} = \mu\left(\frac{\partial v}{\partial x} + \frac{\partial u}{\partial z}\right) = f_5(\mu) \tag{2.5}$$

Here $\rho(x, z)$ is the mass density, $\mu(x, z)$, and $\lambda(x, z)$ are the Lame's coefficients of the material. The equations 2.1-2.5 can be written as

$$F(\rho(x, z), \mu(x, z), \lambda(x, z)) = \mathbf{d}. \tag{2.6}$$

To solve the above wave equations numerically, specific boundary conditions are needed. We impose three boundary conditions: the free surface boundary condition on the top of the domain, the absorbing boundary condition on the right side of the domain and bottom of the domain, and the symmetric boundary condition on the left-hand side of the domain.

2.1.1 Free Surface Boundary Conditions

The measurements of the wavefield are generally collected along the earth's subsurface. Therefore, we impose the free surface boundary condition on the top of the domain by setting the vertical stress components are as zero.

$$\begin{cases} \sigma_{xz} = 0 \\ \sigma_{zz} = 0. \end{cases} \tag{2.7}$$

2.1.2 Absorbing Boundary Conditions

Numerical methods are solved for a region of space by imposing artificial boundaries. Therefore, to avoid the reflections from the boundaries, absorbing boundary conditions should be applied on the right-hand side and the bottom of the domain. Thus the absorbing condition at the bottom of the domain is

$$\begin{cases} \frac{\partial u}{\partial t} + V_s\frac{\partial u}{\partial z} = 0 \\ \frac{\partial v}{\partial t} + V_p\frac{\partial v}{\partial z} = 0 \end{cases} \tag{2.8}$$

and at the right-hand side of the domain

$$\begin{cases} \frac{\partial u}{\partial t} + V_s\frac{\partial u}{\partial x} = 0 \\ \frac{\partial v}{\partial t} + V_p\frac{\partial v}{\partial x} = 0, \end{cases} \tag{2.9}$$

where V_s and V_p are sheer and pressure wave velocities, respectively.

2.1.3 Symmetric Condition

To save computational time, we imposed a symmetric condition along the load line. Thus at the left-hand side of the domain we set

$$\begin{cases} \sigma_{xz} = 0 \\ u = 0. \end{cases} \tag{2.10}$$

To solve these equations, one can use numerical approaches such as finite difference method, finite element method, and Fourier/spectral method. Ref. Tran & McVay (2012) used a classic velocity-stress staggered-grid finite-difference solution of the 2-D elastic wave equations in the time domain (Virieux, 1986) with the absorbing boundary conditions (Clayton and Engquist, 1977). In that approach, a direct discretization of the equations 2.1-2.5, both in time and in space is considered.

2.2 A Classic Finite Difference Scheme

To solve Equations 2.1-2.5 with the above boundary conditions 2.7 - 2.10, the derivatives are discretized using central finite differences. For a field variable f, the temporal finite difference discretization is

$$D_t \left[f\right]_{i,j}^{k} = \frac{f_{i,j}^{k+1/2} - f_{i,j}^{k-1/2}}{\delta t} = \frac{\partial f}{\partial t}|_{i,j}^{k} + \mathcal{O}(\delta^{\in}) \tag{2.11}$$

and the spatial discretizations we choose are,

$$D_x \left[f\right]_{i,j}^{k} = \frac{f_{i+1/2,j}^{k} - f_{i-1/2,j}^{k}}{h_1} = \frac{\partial f}{\partial x}|_{i,j}^{k} + \mathcal{O}(\langle_{\infty}^{\in}) \tag{2.12}$$

$$D_z \left[f\right]_{i,j}^{k} = \frac{f_{i,j+1/2}^{k} - f_{i,j-1/2}^{k}}{h_3} = \frac{\partial f}{\partial z}|_{i,j}^{k} + \mathcal{O}(\langle_{\ni}^{\in}), \tag{2.13}$$

where $\mathcal{O}\left(\cdot\right)$ is the local truncation error. Here i, j, and k represent the indices used in the discretization for the directions x, y and time. The domain is discretized in the x, y and time directions, as shown in Fig. 1. Here, h_1, h_3, and δt are the grid steps for x, z and time directions, respectively. The function f can take $u, v, \sigma_{xx}, \sigma_{zz}, \sigma_{xz}$. For example, the derivative terms $\frac{\partial u}{\partial t}$, $\frac{\partial \sigma_{xx}}{\partial x}$, and $\frac{\partial \sigma_{xz}}{\partial z}$ in Eq. 2.1 can be approximated as

$$\frac{\partial u}{\partial t} = \frac{u_{i,j}^{k+1/2} - u_{i,j}^{k-1/2}}{2\delta t} \tag{2.14}$$

$$\frac{\partial \sigma_{xx}}{\partial x} = \frac{{\sigma_{xx}}_{i+1/2,j}^{k} - {\sigma_{xx}}_{i-1/2,j}^{k}}{2h_1} \tag{2.15}$$

$$\frac{\partial \sigma_{xz}}{\partial z} = \frac{{\sigma_{xz}}_{i,j+1/2}^{k} - {\sigma_{xz}}_{i,j-1/2}^{k}}{2h_3} \tag{2.16}$$

Then, Eq. 2.1 can be approximated using Eqs. 2.14, 2.15, and 2.16 as,

$$\frac{u_{i,j}^{k+1/2} - u_{i,j}^{k-1/2}}{2\delta t} = \frac{1}{\rho}\left(\left(\frac{{\sigma_{xx}}_{i+1/2,j}^{k} - {\sigma_{xx}}_{i-1/2,j}^{k}}{2h_1}\right)\left(\frac{{\sigma_{xz}}_{i,j+1/2}^{k} - {\sigma_{xz}}_{i,j-1/2}^{k}}{2h_3}\right)\right) \tag{2.17}$$

Equations 2.18 - 2.22 are the second order accuracy numerical scheme after discretizing the system of differential equations, (Virieux, 1986). The velocity field $(U, V) = (u, v)$ at time $\left(k + \frac{1}{2}\right)\delta t$ and the stress-tensor field $(T_{xx}, T_{zz}, T_{xz}) = (\sigma_{xx}, \sigma_{zz}, \sigma_{xz})$ at time $(k+1)\,\delta t$ are explicitly calculated with the numerical scheme.

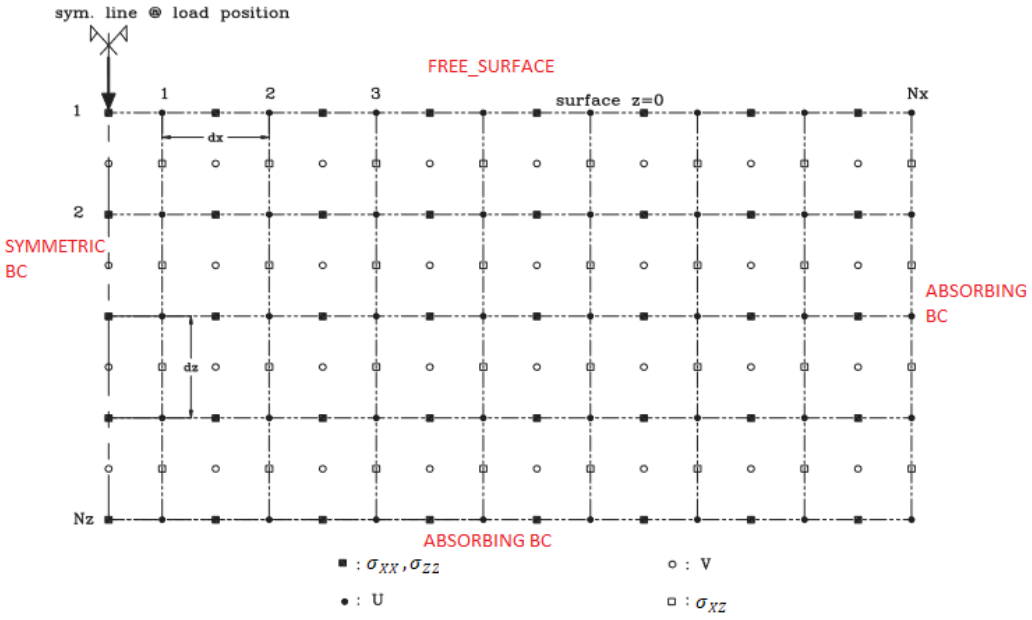

Figure 1: The discretization of the domain (photo credit: Ref. Tran & McVay (2012)).

$$U_{i,j}^{k+1/2} = U_{i,j}^{k-1/2} + B_{i,j}\frac{\delta t}{h_1}\left(Txx_{i+1/2,j}^{k} - Txx_{i-1/2,j}^{k}\right) + B_{i,j}\frac{\delta t}{h_3}\left(Txz_{i,j+1/2}^{k} - Txz_{i,j-1/2}^{k}\right) \tag{2.18}$$

$$\begin{aligned} V_{i+1/2,j+1/2}^{k+1/2} &= V_{i+1/2,j+1/2}^{k-1/2} + B_{i+1/2,j+1/2}\frac{\delta t}{h_1}\left(Txz_{i+1,j+1/2}^{k} - Txz_{i,j+1/2}^{k}\right) \\ &+ B_{i+1/2,j+1/2}\frac{\delta t}{h_3}\left(Tzz_{i+1/2,j+1}^{k} - Txz_{i+1/2,j}^{k}\right) \end{aligned} \tag{2.19}$$

$$\begin{aligned} Txx_{i+1/2,j}^{k+1} &= Txx_{i+1/2,j}^{k} + (L+2M)_{i+1/2,j}\frac{\delta t}{h_1}\left(U_{i+1,j}^{k+1/2} - U_{i,j}^{k+1/2}\right) \\ &+ L_{i+1/2,j}\frac{\delta t}{h_3}\left(V_{i+1/2,j+1/2}^{k+1/2} - U_{i+1/2,j-1/2}^{k+1/2}\right) \end{aligned} \tag{2.20}$$

$$\begin{aligned} Tzz_{i+1/2,j}^{k+1} &= Tzz_{i+1/2,j}^{k} + (L+2M)_{i+1/2,j}\frac{\delta t}{h_1}\left(V_{i+1/2,j+1/2}^{k+1/2} - V_{i+1/2,j-1/2}^{k+1/2}\right) \\ &+ L_{i+1/2,j}\frac{\delta t}{h_3}\left(U_{i+1,j}^{k+1/2} - U_{i,j}^{k+1/2}\right) \end{aligned} \tag{2.21}$$

$$\begin{aligned} Txz_{i,j+1/2}^{k+1} &= Txz_{i,j+1/2}^{k} + M_{i,j+1/2}\frac{\delta t}{h_3}\left(U_{i,j+1}^{k+1/2} - U_{i,j}^{k+1/2}\right) \\ &+ M_{i,j+1/2}\frac{\delta t}{h_1}\left(V_{i+1/2,j+1/2}^{k+1/2} - V_{i-1/2,j+1/2}^{k+1/2}\right) \end{aligned} \tag{2.22}$$

Here, M and L represent the Lame coefficients (μ, λ) and

$$B = \frac{1}{\rho} \tag{2.23}$$

as shown in Fig. 1.

Moreover, the initial condition at time $t = 0$ is set such that the stress and velocity are zero everywhere in the domain. The medium is perturbed by changing vertical stress σ_{zz} at the source using

$$R(t) = \left[1 - 2\pi^2 f_c^2 (t - t_0)^2\right] \exp\left[-\pi^2 f_c^2 (t - t_0)^2\right], \tag{2.24}$$

where f_c is the center of the frequency band and t_0 is the time shift.

2.2.1 Stability Criterion

Numerical schemes are generally associated with numerical errors due to the approximation of the derivatives in the partial differential scheme. It is important to obtain a stable wave propagation solution from the finite difference scheme. With some numerical schemes, the errors made at one-time step grow as the computations proceed. Such a numerical scheme is said to be unstable so the results blow up. If the errors decay with time as the computations proceed, we say a finite difference scheme is stable. In that case, the numerical solutions are bounded.

To obtain a bounded solution from the finite difference scheme, we obtain δt from the stability criterion (Virieux, 1986) given by

$$\delta t \leq \frac{1}{V_{\text{max}} \sqrt{\frac{1}{h_1^2} + \frac{1}{h_3^2}}}. \tag{2.25}$$

Here V_{max} is the maximum P-wave velocity in the media.

Inputs for the forward problem are the model parameters such as density, Lames's moduli, P-wave velocity, and S-wave velocity. Then the particle velocities and stresses (outputs) are calculated by implementing the numerical scheme (Eqs. 2.18 - 2.22) in MATlab.

3 Non-uniform mesh refinement method

In this section, we present the non-uniform mesh refinement method proposed in Ref. Kostin et al. (2015) with some modification for spatial mesh refinement. Ref. Kostin et al. (2015) used fast Fourier interpolation for spatial mesh refinement, but here we use a cubic spline interpolation, which we find better control of smoothing regularity.

The domain is categorized into a coarse grid and a fine grid. The coarse grid is the regular grid that we introduce in Section 2.2. Regular grids are considered with integer and half-integer points. The time grid and the spatial grid are denoted by $T^C = \left\{t^N | N = 0, 1/2, 1, ...\right\}$ and $\Omega^C = \left\{\left((x)_I, (z)_J\right) | I = 0, \pm 1/2, \pm 1, ...; J = 0, \pm 1/2, \pm 1, ...\right\}$, respectively. The grid steps with respect to time and the spatial directions x and z are τ, h_1, and h_3, respectively. The sub-grids are introduced so that they do not intersect with each other. Figure 2 shows a sketch of the staggered grid scheme.

The sub grids in the staggered grid can be introduced as

$$T_\sigma^C = \left\{t^{n+1/2} | n \in \mathbb{N}\right\}, T_{u,v}^C = \left\{t^n | n \in \mathbb{N}\right\} \tag{3.1}$$

$$\Omega_{\sigma_{xx}}^C = \Omega_{\sigma_{zz}}^C = \left\{\left((x)_i, (z)_j\right) | i \in \mathbb{Z}, j \in \mathbb{Z}\right\}, \tag{3.2}$$

$$\Omega_{\sigma_{xz}}^C = \left\{\left((x)_{i+1/2}, (z)_{j+1/2}\right) | i \in \mathbb{Z}, j \in \mathbb{Z}\right\}, \tag{3.3}$$

$$\Omega_u^C = \left\{\left((x)_{i+1/2}, (z)_j\right) | i \in \mathbb{Z}, j \in \mathbb{Z}\right\}, \tag{3.4}$$

$$\Omega_v^C = \left\{\left((x)_i, (z)_{j+1/2}\right) | i \in \mathbb{Z}, j \in \mathbb{Z}\right\}. \tag{3.5}$$

The fine grid is introduced in such a way that the coarse grid is a subset of the fine grid. Two sub grids for velocity fields and the stress tensor fields with respect to time in the fine zone are defined.

(2)

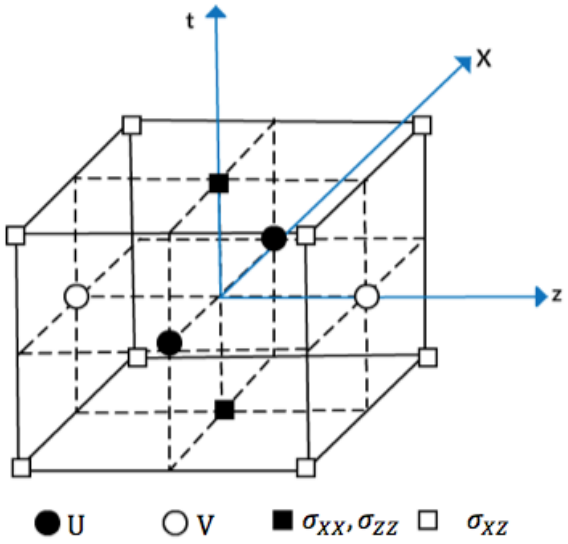

Figure 2: The grid structure for the standard staggered grid scheme.

The refinement ratio with respect to time is taken as K.

$$T_{\sigma}^{F} = \left\{ t^{n+\frac{1}{2}+\frac{k}{K}} | n \in \mathbb{N}, k = 1, ..., K \right\} \tag{3.6}$$

$$T_{u,v}^{F} = \left\{ t^{n+\frac{k}{K}} | n \in \mathbb{N}, k = 1, ..., K \right\} \tag{3.7}$$

$$T^{F} = T_{\sigma}^{F} + T_{u}^{F} \tag{3.8}$$

The fine grid with respect to space for field variables can be introduced as

$$\Omega_{\sigma_{xx}}^{F} = \Omega_{\sigma_{zz}}^{F} = \left\{ \left((x)_{i+l_1/L_1}, (z)_{j+l_3/L_3} \right) | i \in \mathbb{Z}, j \in \mathbb{Z} \right\}, \tag{3.9}$$

$$\Omega_{\sigma_{xz}}^{F} = \left\{ \left((x)_{i+1/2+l_1/L_1}, (z)_{j+1/2+l_3/L_3} \right) | i \in \mathbb{Z}, j \in \mathbb{Z} \right\}, \tag{3.10}$$

$$\Omega_{u}^{F} = \left\{ \left((x)_{i+1/2+l_1/L_1}, (z)_{j+l_3/L_3} \right) | i \in \mathbb{Z}, j \in \mathbb{Z} \right\}, \tag{3.11}$$

$$\Omega_{v}^{F} = \left\{ \left((x)_{i+l_1/L_1}, (z)_{j+1/2+l_3/L_3} \right) | i \in \mathbb{Z}, j \in \mathbb{Z} \right\}, \tag{3.12}$$

for $l_1 = 1, ..., L_1$ and $l_3 = 1, ..., L_3$.

$$\Omega^{F} = \Omega_{\sigma_{xx}}^{F} + \Omega_{\sigma_{xz}}^{F} + \Omega_{u}^{F} + \Omega_{v}^{F} \tag{3.13}$$

where L_1 and L_3 are the refinement ratios with respect to the spatial directions in x and z. The refinement ratios K, L_1, and L_3 are taken to be odd numbers, which ensures the consistency of all sub grids.

The transition zone is introduced when switching from coarse grid to the fine grid. A sketch of the refined grid for the standard staggered grid scheme is shown in Fig.3.

The refinements are introduced in the following ranges along the spatial direction z:

(3)

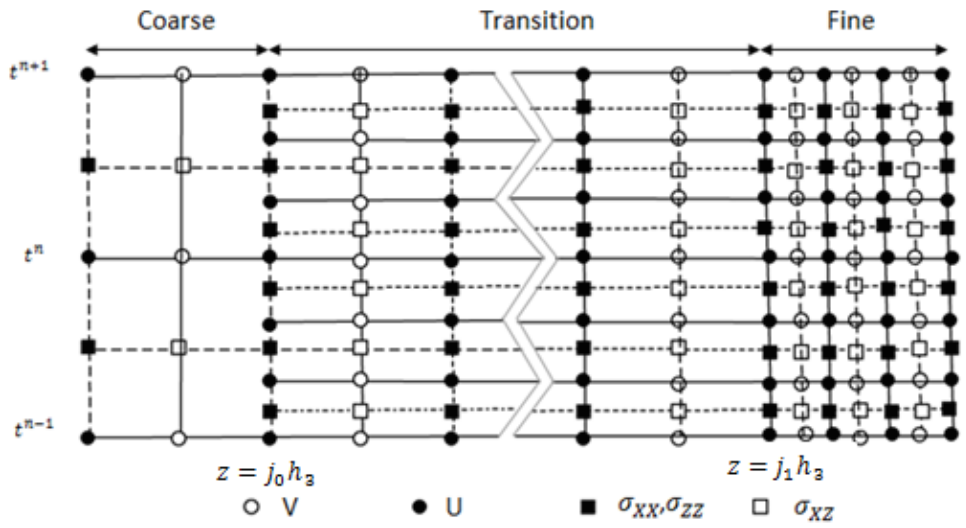

Figure 3: A sketch of the refined grid for the standard staggered grid scheme.

- a coarse zone - $z < j_0 h_3$, where j_0 is is an integer. Both time and space are coarse in this zone.
- a transition zone - $j_0 h_3 < z < j_1 h_3$, where j_0 is an integer and j_1 is an half integer. In this zone, coarse grid in space and fine grid in time are used.
- a fine zone - $z < j_1 h_3$. In this zone, both a fine grid in time and space are used.

The grid functions of the field variables can be defined as the cross product of time and the corresponding spatial domains.

3.1 Wave equation discretization

We discretize the wave equation by the following central difference schemes. This approximation scheme has of second order accuracy. The Finite difference operations, which are defined on the filed variable f for the coarse grid are given by

$$D_t^C [f]_{I,J}^N = \frac{f_{I,J}^{N+1/2} - f_{I,J}^{N-1/2}}{\tau} = \frac{\partial f}{\partial t}|_{I,J}^N + O(\tau^2) \tag{3.14}$$

$$D_x^C [f]_{I,J}^N = \frac{f_{I+1/2,J}^N - f_{I-1/2,J}^N}{h_1} = \frac{\partial f}{\partial x}|_{I,J}^N + O(h_1^2) \tag{3.15}$$

$$D_z^C [f]_{I,J}^N = \frac{f_{I,J+1/2}^N - f_{I,J-1/2}^N}{h_3} = \frac{\partial f}{\partial z}|_{I,J}^N + O(h_3^2). \tag{3.16}$$

Here, f represents $u, v, \sigma_{XX}, \sigma_{ZZ}$, and σ_{XZ}.

The finite difference operations acting on the fine grid are

$$D_t^F\,[f]_{I,J}^N = \frac{f_{I,J}^{N+1/2K} - f_{I,J}^{N-1/2K}}{\tau/K} = \frac{\partial f}{\partial t}|_{I,J}^N + O(\tau^2) \tag{3.17}$$

$$D_x^F\,[f]_{I,J}^N = \frac{f_{I+1/2L_1,J}^N - f_{I-1/2L_1,J}^N}{h_1/L_1} = \frac{\partial f}{\partial x}|_{I,J}^N + O(h_1^2) \tag{3.18}$$

$$D_z^F\,[f]_{I,J}^N = \frac{f_{I,J+1/2L_3}^N - f_{I,J-1/2L_3}^N}{h_3/L_3} = \frac{\partial f}{\partial z}|_{I,J}^N + O(h_3^2). \tag{3.19}$$

In order to obtain bounded solutions, we need to employ the stability criterion

$$\tau \leq \frac{1}{V_{\max}\sqrt{\frac{1}{h_1^2} + \frac{1}{h_3^2}}}, \tag{3.20}$$

where V_{max} is the maximum of the P-wave velocity. Thus in the transition zone, successive mesh refinement is used. Therefore, the fine grid at time T^F and the coarse spatial grid, Ω^C, are used. The finite difference operators, acting on the transition zone are

$$D_t^F\,[f]_{I,J}^N = \frac{f_{I,J}^{N+1/2K} - f_{I,J}^{N-1/2K}}{\tau/K} = \frac{\partial f}{\partial t}|_{I,J}^N + \mathcal{O}(\tau^{\in}) \tag{3.21}$$

$$D_x^C\,[f]_{I,J}^N = \frac{f_{I+1/2,J}^N - f_{I-1/2,J}^N}{h_1} = \frac{\partial f}{\partial x}|_{I,J}^N + \mathcal{O}(\langle_{\infty}^{\in}) \tag{3.22}$$

$$D_z^C\,[f]_{I,J}^N = \frac{f_{I,J+1/2}^N - f_{I,J-1/2}^N}{h_3} = \frac{\partial f}{\partial z}|_{I,J}^N + \mathcal{O}(\langle_{\ni}^{\in}) \tag{3.23}$$

3.2 Refinement of Solutions at Interfaces

For a smooth transition from coarse to fine, the transition zone is introduced. At the same time, solutions at the interfaces $z = j_0 h_3$ and $z = j_1 h_3$ should be updated in a special manner for smooth transition. The solutions at the interface $z = j_0 h_3$ are calculated before updating the solutions at the transition zone. At the interface $z = j_0 h_3$, only time need to be fined. Similarly, solutions at the interface $z = j_1 h_3$ are calculated before updating the solutions in the fine zone.

3.2.1 Refinement of temporal steps at the interface $z = j_0 h_3$

In the interface $z = j_0 h_3$, time interval $[t^n, t^{n+1}]$ can be divided as $t \in (t^n, t^{n+1/2}]$and $t \in (t^{n+1/2}, t^{n+1}]$ for an integer n. Figure 4 shows the section of the time grid at the interface $z = j_0 h_3$. Then solution is updated separately inside the sub-time interval. Note that the time step in the coarse grid and fine grid are τ and τ/K for a positive, odd integer, K. Since only the temporal refinement occurs in the transition zone, the time step for the transition zone is τ/K.

3.2.2 The time interval $t \in (t^n, t^{n+1/2}]$

Since j_0 is an integer, only the diagonal component of the stress sensors σ_{XX} and σ_{ZZ} are updated at the interface. These stress sensors should be updated at the instances $t^{n+(2k-1)/2K}$ for $k = 1, 2, ..., (K+1)/2$. Approximations for the stress tensor at the interface $j_0 h_3$ are obtained as

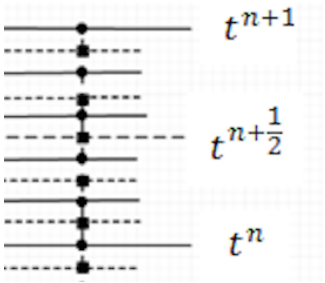

Figure 4: A section of the time grid

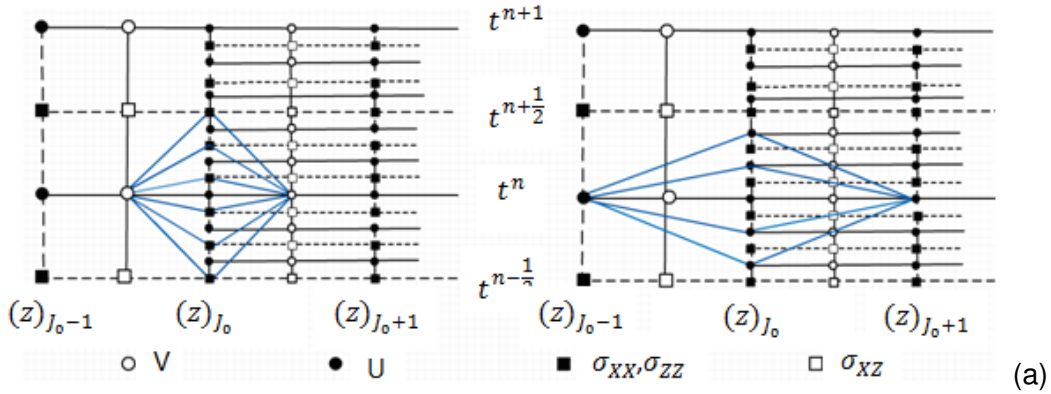

(a)

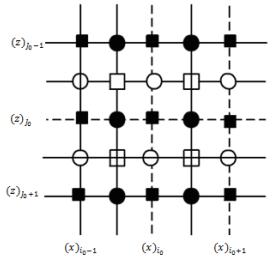

(b)

Figure 5: 2D (t, z) projection of embedded stencils used to update the solution from the instant t^n to $t^{n+1/2}$. (a) update of stresses at the interface (b) Spatial staggered grid stencil used to update velocity component

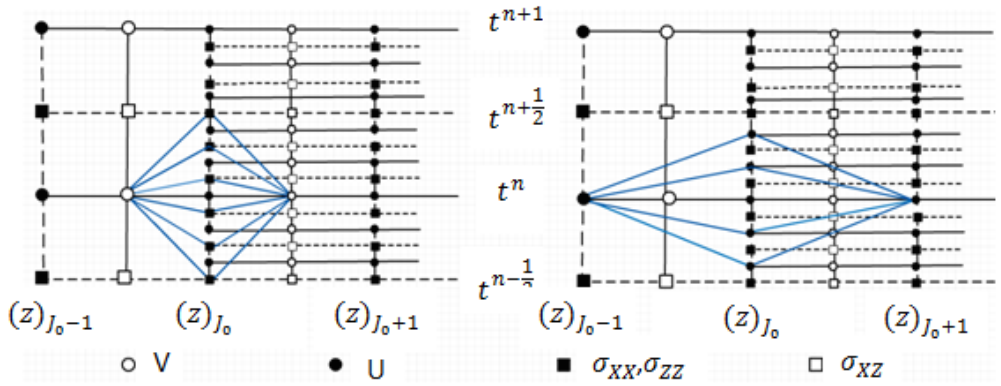

(a)

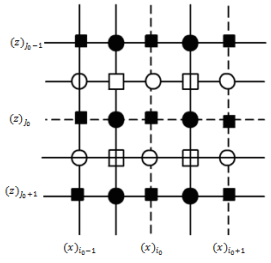

(b)

Figure 6: 2D (t, z) projection of embedded stencils used to update the solution from the instant t^n to $t^{n+1/2}$. (a) update of stresses at the interface (b) Spatial staggered grid stencil used to update velocity component

$$\frac{(\sigma_{xx})_{i,J_0}^{n+\frac{2k-1}{K}} - (\sigma_{xx})_{i,J_0}^{n-\frac{2k-1}{K}}}{(2k-1)\frac{\tau}{2K}} = (\hat{\lambda}_{i,J_0} + 2\hat{\mu}_{i,J_0}) D_1^C [u]_{i,J_0}^n + \hat{\lambda}_{i,J_0} D_3^C [v]_{i,J_0}^n \tag{3.24}$$

$$\frac{(\sigma_{zz})_{i,J_0}^{n+\frac{2k-1}{K}} - (\sigma_{zz})_{i,J_0}^{n-\frac{2k-1}{K}}}{(2k-1)\frac{\tau}{2K}} = \hat{\lambda}_{i,J_0} D_1^C [u]_{i,J_0}^n + (\hat{\lambda}_{i,J_0} + 2\mu_{i,J_0}) D_3^C [v]_{i,J_0}^n \tag{3.25}$$

for $k = 1, ..., (K+1)/2$. The velocity vector component is updated at the interface $z = j_0 h_3$ using the finite difference approximation of the equation,

$$\rho \frac{\partial^2 u}{\partial t^2} = \frac{\partial}{\partial x}\left((\lambda + \mu)\frac{\partial u}{\partial x} + \lambda \frac{\partial v}{\partial z}\right) + \frac{\partial}{\partial z}\left(\mu \frac{\partial v}{\partial x} + \mu \frac{\partial v}{\partial z}\right). \tag{3.26}$$

3.2.3 The time interval $t \in (t^n, t^{n+1/2}]$

Since j_0 is an integer, only the diagonal component of the stress sensors σ_{XX} and σ_{ZZ} are updated at the interface. These stress sensors should be updated at the instances $t^{n+(2k-1)/2K}$ for $k = 1, 2, ..., (K+1)/2$. Approximations for the stress tensor at the interface $j_0 h_3$ are obtained as

$$\frac{(\sigma_{xx})_{i,J_0}^{n+\frac{2k-1}{K}} - (\sigma_{xx})_{i,J_0}^{n-\frac{2k-1}{K}}}{(2k-1)\frac{\tau}{2K}} = (\hat{\lambda}_{i,J_0} + 2\hat{\mu}_{i,J_0}) D_1^C [u]_{i,J_0}^n + \hat{\lambda}_{i,J_0} D_3^C [v]_{i,J_0}^n \tag{3.27}$$

$$\frac{(\sigma_{zz})_{i,J_0}^{n+\frac{2k-1}{K}} - (\sigma_{zz})_{i,J_0}^{n-\frac{2k-1}{K}}}{(2k-1)\frac{\tau}{2K}} = \hat{\lambda}_{i,J_0} D_1^C [u]_{i,J_0}^n + (\hat{\lambda}_{i,J_0} + 2\mu_{i,J_0}) D_3^C [v]_{i,J_0}^n \tag{3.28}$$

for $k = 1, ..., (K+1)/2$. The velocity vector component is updated at the interface $z = j_0 h_3$ using the finite difference approximation of the equation,

$$\rho \frac{\partial^2 u}{\partial t^2} = \frac{\partial}{\partial x}\left((\lambda + \mu)\frac{\partial u}{\partial x} + \lambda \frac{\partial v}{\partial z}\right) + \frac{\partial}{\partial z}\left(\mu \frac{\partial v}{\partial x} + \mu \frac{\partial v}{\partial z}\right). \tag{3.29}$$

3.2.4 The time interval $t \in (t^{n+1/2}, t^{n+1}]$

In the time interval $t \in (t^{n+1/2}, t^{n+1}]$, the velocity and the stress tensors are updated with the following equations:

$$\hat{\rho}_{i+\frac{1}{2},J_0} \frac{(u)_{i+\frac{1}{2},J_0}^{n+\frac{1}{2}+\frac{2k-1}{2K}} - (u)_{i+\frac{1}{2},J_0}^{n+\frac{1}{2}-\frac{2k-1}{2K}}}{(2k-1)\frac{\tau}{2K}} = D_1^C [\sigma_{xx}]_{i+\frac{1}{2},J_0}^{n+\frac{1}{2}} + D_3^C [\sigma_{zz}]_{i+\frac{1}{2},J_0}^{n+\frac{1}{2}}, \tag{3.30}$$

for $k = 1, ..., (K+1)/2$.

$$\frac{\partial^2 \sigma_{xx}}{\partial t^2} = (\lambda + 2\mu)\frac{\partial}{\partial x}\left(\frac{1}{\rho}\frac{\partial \sigma_{xx}}{\partial x} + \frac{1}{\rho}\frac{\partial \rho_{xz}}{\partial z}\right) + \lambda\left(\frac{1}{\rho}\frac{\partial \sigma_{xz}}{\partial x} + \frac{1}{\rho}\frac{\partial \sigma_{zz}}{\partial z}\right) \tag{3.31}$$

$$\frac{\partial^2 \sigma_{xx}}{\partial t^2} = \lambda\frac{\partial}{\partial x_1}\left(\frac{1}{\rho}\frac{\partial \sigma_{xx}}{\partial x} + \frac{1}{\rho}\frac{\partial \rho_{xz}}{\partial z}\right) + (\lambda + 2\mu)\left(\frac{1}{\rho}\frac{\partial \sigma_{xz}}{\partial x} + \frac{1}{\rho}\frac{\partial \sigma_{zz}}{\partial z}\right) \tag{3.32}$$

3.2.5 Refinement of the spatial steps at the interface, $j_1 h_3$

The interface $j_1 h_3$ appears between the transition zone and the fine grid zone. Notice that j_1 is a half-integer number. The step size of the spatial direction in the transition zone are h_1 and h_3. Also, space grid in the transition zone is a coarse grid. Thus the step sizes of the fine grid are taken as $h_1/L1$ and h_3/L_3 where L_1 and L_2 are refinement ratios in the x and z direction. To update the solution at the interface $j_1 + \frac{1}{2L_3}$ from the coarse to the fine grid, the following equations are obtained using the finite-difference approximation.

$$\hat{\rho}_{I,J_1+\frac{1}{2L_3}}^N D_t^F [v]_{I,J_1+\frac{1}{2L_3}}^N = D_1^F [\sigma_{xz}]_{I,J_1+\frac{1}{2L_3}}^N + D_3^F [\tilde{\sigma}_{zz}]_{I,J_1+\frac{1}{2L_3}}^N \tag{3.33}$$

$$D_t^F [\sigma_{xz}]_{I,J_1+\frac{1}{2L_3}}^N = \hat{\mu}_{I,J_1+\frac{1}{2L_3}}^N \left(D_1^F [v]_{I,J_1+\frac{1}{2L_3}}^N + D_3^F [\tilde{u}]_{I,J_1+\frac{1}{2L_3}}^N\right), \tag{3.34}$$

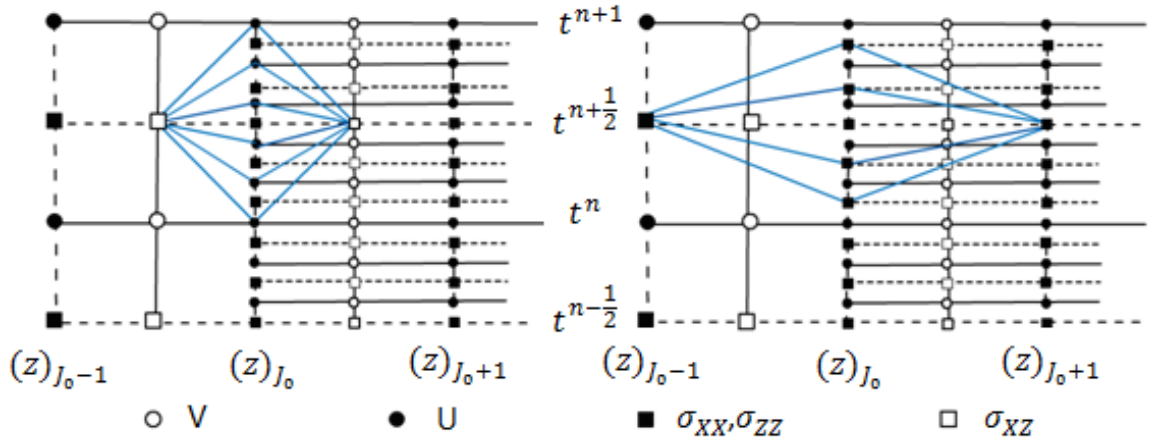

Figure 7: 2D (t, z) projection of embedded stencils used to update the solution from the instant $t^{n+1/2}$ to t^{n+1}. Stress component at the interface is updated with the stencil.

In the above equations, $\sigma_{\tilde{Z}Z}$ and $\tilde{u}$ indicates that the up sampling of the variables σ_{ZZ} and u is required along the interface $j_1 h_3$. These components are defined on the line $z = j_1 h_3$ as shown in Fig. 8. Thus the 1D interpolation is needed to get these components in the fine grid due to the shift of the grids. Ref. Kostin et al. (2015) applied a fast Fourier transform for the interpolation. However, we use the cubic smoothing spline Pollock et al. (1993); Reinsch (1967) for the interpolation.

3.3 Cubic smoothing spline Interpolation

For a given a set of co-ordinates (x_i, y_i), for $i = 1, 2, ..., n$ of a function $y = f(x)$,a cubic spline finds a curve that connects the gap between the two adjacent points (x_j, y_j) and (x_{j+1}, y_{j+1}). The cubic spline approach uses cubic functions S_i, $i = 1, 2, .., n-1$ and their first and second derivatives.

The cubic function can be expressed as

$$S_i(x) = a_i (x - x_i)^3 + b_i (x - x_i)^2 + c_i (x - x_i) + d_i, \tag{3.35}$$

where $x_i \leq x \leq x_{i+1}$.

In the case of interests of smoothness, one can consider the coordinates of the data given by

$$y_i = f(x_i) + \epsilon_i, \tag{3.36}$$

where ϵ_i, $i = 0, 1, ..., n$ represents the noise of the curve and a random variable with variance σ_i^2. Thus the spline is smoothed. The function $f(x)$ can be obtained by constructing a spline function, $S(x)$, which minimizes the function

$$L = \lambda \sum_{i=0}^{n} \left(\frac{y_i - S_i}{\sigma_i} \right)^2 + (1 - \lambda) \int_{x_0}^{x_n} \left(S''(x) \right)^2 dx, \tag{3.37}$$

where $S_i = S(x_i)$ and λ is the smoothing parameter or penalty for the roughness of the function.

Here, the first term considers reducing the error between the spline and the data points. So the spline should come reasonably close to the data. The second term considers the low curvature of

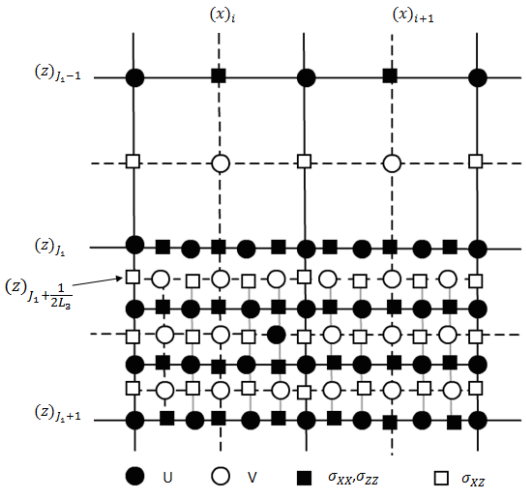

Figure 8: The grid of the spatial mesh refinement interface $(x_3)_{J_1}$.

the spline. Thus the smoothing spline Eq. 3.37 produces a spline that balances these two opposing criteria.

We implement the above refinement procedure with the defined boundary conditions in Eqs. 2.7 - 2.10, the initial condition in Eq. 2.24, and the stability criterion 3.20 in MAT lab.

4 Wave Propagation Results

In this section, we present the wave propagation results from the above method. A numerical study was conducted with 2-D domain of size 50 m $\times$ 50 m. Step sizes in the spatial directions in the regular grid are taken as $h_1 = h_3 = 0.5$. Thus a 100×100 regular mesh in the spatial domain is created. The time step τ is calculated with the stability criterion (Eq. 3.20) using the maximum P- wave velocity. The shear wave velocity V_s of the medium was considered as 200 m/s. The pressure wave velocity V_p was calculated using the defined shear wave velocity and the formula

$$V_p = V_s \sqrt{\left(\frac{2\,(1-\nu)}{1-2\nu}\right)}, \tag{4.1}$$

where $\nu = 0.33$ is used in the numerical calculations. The density of the medium is considered to be 1800 m/s. A source was located at the grid point (1,50) in the spatial domain. 20 receivers were positioned in the domain with the 2.5 m spacing on the surface. Thus, the source was placed 24 m away from the first receiver.

The time refinement and spatial refinement ratios are as $K, L_1, L_3 = 3$. A refinement area in the grid was considered from 6m to 15m in the z direction. Accordingly, the coarse zone, transition zone, and fine grid zone are defined in Table 1 and Fig. 9.

Here, we introduced two transition zones. The first transition zone appears when the wave propagates from coarse to fine and the second transition zone appears when the wave propagates from fine to coarse grid zone. The wave fields were obtained from the classic finite difference approach using the uniform mesh and the mesh refinement approach (non uniform mesh) to see

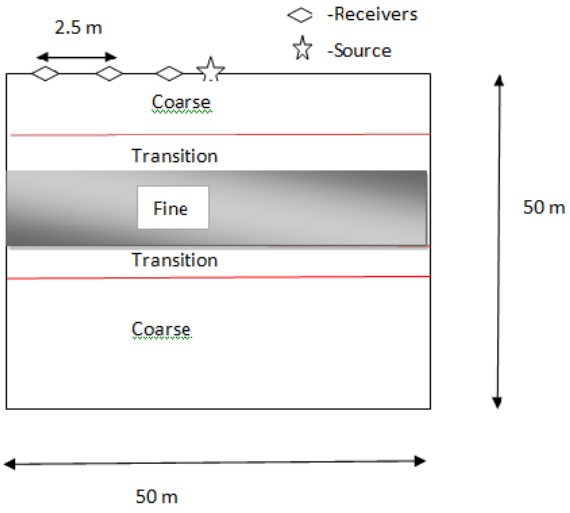

Figure 9: Grid cells breakdown

Table 1: Grid cells breakdown in the grid zones

grid zone	grid cells
coarse	1-10
transition	10-12
fine	12-30
transition	30-32
coarse	32-100

the accuracy of the presented method. Figure 10 shows the wave fields obtained at three depths, 0.5m, 6.5 m, and 16.5 m depths at the receivers. Note that these three depths are positions in the coarse grid (before the transition zone to the fine grid), fine grid, and coarse grid (after the transition zone to the fine grid), respectively.

Figure 10 shows the estimated wave field at receivers. Figure 10 (a),(c), and (e) corresponding to the observed wavefield data from the mesh grid method and Fig. 10 (b),(d), and (f) correspond to the estimated field data from the classic finite difference method. One can see that results from both methods are the same at receivers at the same depth. However, an advantage of the mesh refinement method is the ability of simulation real models with small-scale heterogeneities. In this study, we only consider the ability to estimate wavefield data from the mesh refinement method. Also, the mesh refinement method is able to be applied with different refinement ratios at different surfaces. In this case, the fine grid zone has the refinement ratios of $L_1 = L_3 = 3$ for x, z directions. The step sizes in the fine grid zone are $h_1/L_1 = 1/6$ and $h_3/L_3 = 1/6$. Thus the coarse grid zone and the fine grid zone behave as two layers and the mesh refinement is applied only to one layer, which contains small-scale heterogeneities.

Moreover, we compare the computational efficiency of the non-uniform mesh method with the uniform grid method at a smaller step size in spatial directions. The number of cells in the spatial domain for the two methods are shown in Table 2. For example, if the uniform mesh method is used with step size 1/6 (refinement ratio $L_1 = L_3 = 3$) in the x and z directions, the number of grid points in the spatial domain is 90000. However, the spatial domain of the non-uniform mesh refinement method contains only 24400 grid points. Thus less memory storage is required with non-uniform mesh method than the uniform mesh method.

Figure 11 shows the number of grid points in the spatial domain as a function of refinement ratio. The blue color curve represents the number of cells required for the non-uniform mesh method and the red color curve represents the number of cells required for the uniform mesh method. One can see that there are eight orders of magnitude increment in the number of cells with uniform mesh method. However, only 1.5 orders of magnitude increment in the number of cells with the non-uniform mesh method. Therefore, Non-uniform mesh method required less storage even with higher refinement ratio.

Table 2: Domain size of the non uniform mesh method and the uniform grid method at the spatial directions

Refinement Ratio	Number of cells (uniform mesh method)	Number of cells (non-uniform mesh method)
$L_1 = L_3 = 3$ (step size =1/6)	90000	24400
$L_1 = L_3 = 5$ (step size =1/10)	250000	53200

On the other hand, the less computational time is required to generate the wave field using non-uniform mesh method on the same standard computer. In the uniform mesh method, when the refinement ratio increases, Matlab encounters memory problem. This time difference brings the possibility of being applied to the FWI method Tran & McVay (2012) for 3-D large scale problems with small-scale heterogeneities.

Figure 12 shows the wave fields at four receivers at the 6.5m depth using the cubic smoothing spline interpolation method and the finite Fourier transformation method. At the 6.5m depth, the wave propagates in the fine grid area. Thus the spatial mesh refinement is needed. The wave field results using two interpolation methods are compared with the results from the uniform mesh method. Note that we assume the uniform mesh method gives accurate wave field solutions. Figure 12 shows the estimated wave fields only at receiver 6, 9, 12, and 15. Blue, red, and black color curves represent the wave fields using FFT interpolation, cubic smoothing spline interpolation, and the uniform mesh method (without spatial mesh refinement). One can see that, a good agreement between the results from the cubic smoothing spline interpolation and uniform mesh method. However, the solutions with FFT interpolation overestimated the wavefield data.

We calculated the l_2 norm error of the field data with cubic smoothing spline and FFT interpolation. Table 3 shows the l_2 norm error of the two interpolation methods relative to the uniform mesh method at four receivers 6, 9, 12, and 15. Cubic smoothing spline gives less error in the wave field estimation than FFT interpolation.

Receiver	Error (FFT interpolation)	Error (Cubic smoothing spline interpolation)
6	0.55	0.33
9	0.52	0.39
12	0.65	0.51
15	0.65	0.51

Table 3: l_2 norm error of the estimated wave field data using FFT interpolation and cubic smoothing interpolation for spatial mesh refinement

5 Conclusions

In this work, we adopted a method for numerical simulation of wave propagations in media with small scale heterogeneities such as cavities and fractures. This method is introduced by Ref. Kostin et al. (2015) and is based on local mesh refinement with respect to both time and space in different media. One of the main features of their method is the use of fast Fourier transform based interpolation for spatial mesh refinement. In the work, the spatial mesh refinement step has been calculated using cubic smoothing spline interpolation instead of fast Fourier transform. The technique was developed using central finite difference approximation. We presented numerical results for the simulation of seismic wave propagation. The results using the mesh refinement method are compared with a classic finite difference approximation scheme with a uniform mesh. The results of the mesh refinement approach show a good agreement with the results of the wave propagation with the classic finite difference scheme with uniform grid. The advantage of the mesh refinement method is the capability of the simulations of 3-D large scale problems in media with small scale heterogeneities.

Moreover, in the section, results for the wave propagation using the cubic smoothing spline interpolation and fast Fourier interpolation are compared. The mesh refinement method with cubic smoothing spline approach provides better results for wave propagation. Overall, the local time-space mesh refinement approach with the cubic smoothing spline interpolation will be a good candidate for 3-D FWI problem as the ability of the simulation of small scale heterogeneities in different surfaces for large scale problems. In the future, we intend to perform numerical simulations of seismic waves in 3-D heterogeneous media.

References

Appelö, D., & Petersson, N. A. (2009). A stable finite difference method for the elastic wave equation on complex geometries with free surfaces. *Communications in Computational Physics*, *5*(1), 84–107.

Charara, M., Barnes, C., & Tarantola, A. (2000). Full waveform inversion of seismic data for a viscoelastic medium. In *Methods and applications of inversion*, (pp. 68–81). Springer.

Cook, E. R., & Peters, K. (1981). The smoothing spline: a new approach to standardizing forest interior tree-ring width series for dendroclimatic studies.

Crase, E. (1990). High-order (space and time) finite-difference modeling of the elastic wave equation. In *SEG Technical Program Expanded Abstracts 1990*, (pp. 987–991). Society of Exploration Geophysicists.

De Boor, C., De Boor, C., Mathématicien, E.-U., De Boor, C., & De Boor, C. (1978). *A practical guide to splines*, vol. 27. springer-verlag New York.

Di Bartolo, L., Dors, C., & Mansur, W. J. (2012). A new family of finite-difference schemes to solve the heterogeneous acoustic wave equation new finite-difference schemes for acoustics. *Geophysics*, *77*(5), T187–T199.

Ha, W., & Shin, C. (2012). Laplace-domain full-waveform inversion of seismic data lacking low-frequency information. *Geophysics*, *77*(5), R199–R206.

Hou, H., & Andrews, H. (1978). Cubic splines for image interpolation and digital filtering. *IEEE Transactions on acoustics, speech, and signal processing*, *26*(6), 508–517.

Hutchinson, M. (1986). Algorithm 642: A fast procedure for calculating minimum cross-validation cubic smoothing splines. *ACM Transactions on Mathematical Software (TOMS)*, *12*(2), 150–153.

Kosloff, D., Reshef, M., & Loewenthal, D. (1984). Elastic wave calculations by the fourier method. *Bulletin of the Seismological Society of America*, *74*(3), 875–891.

Kostin, V., Lisitsa, V., Reshetova, G., & Tcheverda, V. (2015). Local time–space mesh refinement for simulation of elastic wave propagation in multi-scale media. *Journal of computational physics*, *281*, 669–689.

Lee, K. H., & Kim, H. J. (2003). Source-independent full-waveform inversion of seismic data. *Geophysics*, *68*(6), 2010–2015.

Liang-Guo, D., Zai-Tian, M., Jing-Zhong, C., Hua-Zhong, W., Jian-Hua, G., Bing, L., & Shi-Yong, X. (2000). A staggered-grid high-order difference method of one-order elastic wave equation [j]. *Chinese Journal of Geophysics*, *3*.

Liu, Y., & Sen, M. K. (2009). An implicit staggered-grid finite-difference method for seismic modelling. *Geophysical Journal International*, *179*(1), 459–474.

Pollock, D., et al. (1993). Smoothing with cubic splines.

Reinsch, C. H. (1967). Smoothing by spline functions. *Numerische mathematik*, *10*(3), 177–183.

Sjögreen, B., & Petersson, N. A. (2014). Source estimation by full wave form inversion. *Journal of Scientific Computing*, *59*(1), 247–276.

Tran, K. T., & McVay, M. (2012). Site characterization using gauss–newton inversion of 2-d full seismic waveform in the time domain. *Soil Dynamics and Earthquake Engineering*, *43*, 16–24.

Woodward, M. J. (1992). Wave-equation tomography. *Geophysics*, *57*(1), 15–26.

Xia, F., Dong, L., & Ma, Z. (2004). The numerical modeling of 3-d elastic wave equation using a high-order, staggered-grid, finite difference scheme. *Applied Geophysics*, *1*(1), 38–41.

Xu, S., Wang, D., Chen, F., Zhang, Y., & Lambare, G. (2012). Full waveform inversion for reflected seismic data. In *74th EAGE Conference and Exhibition incorporating EUROPEC 2012*, (pp. cp–293). European Association of Geoscientists & Engineers.

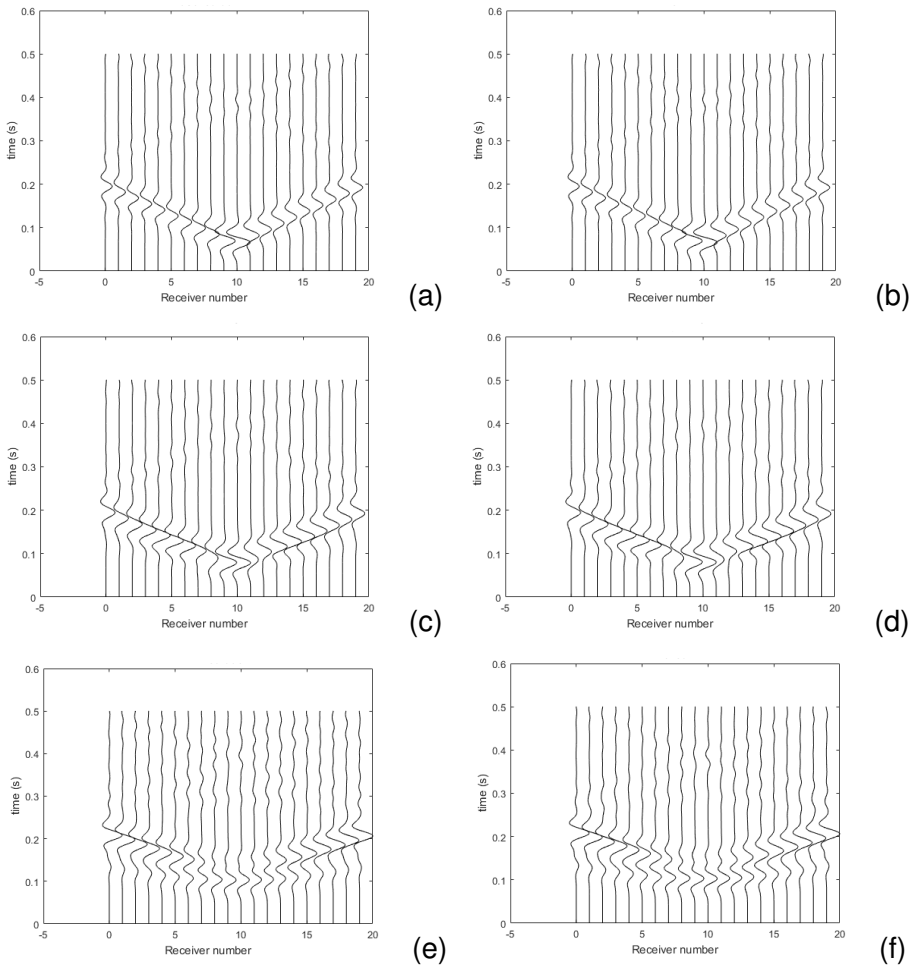

Figure 10: Wave fields from the mesh refinement method (non uniform mesh) at (a) 0.5 m depth, (c) 6.5 m depth, and (e) 16.5 m depth. Wave propagation from the uniform mesh at (b) 0.5 m depth, (d) 6.5 m depth, and (f) 16.5 m depth.

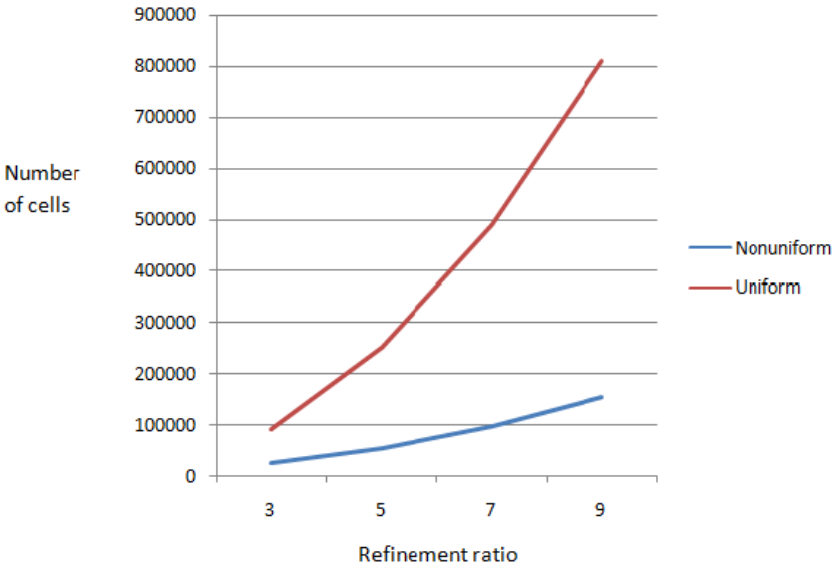

Figure 11: Number of cells as a function of refinement ratio.

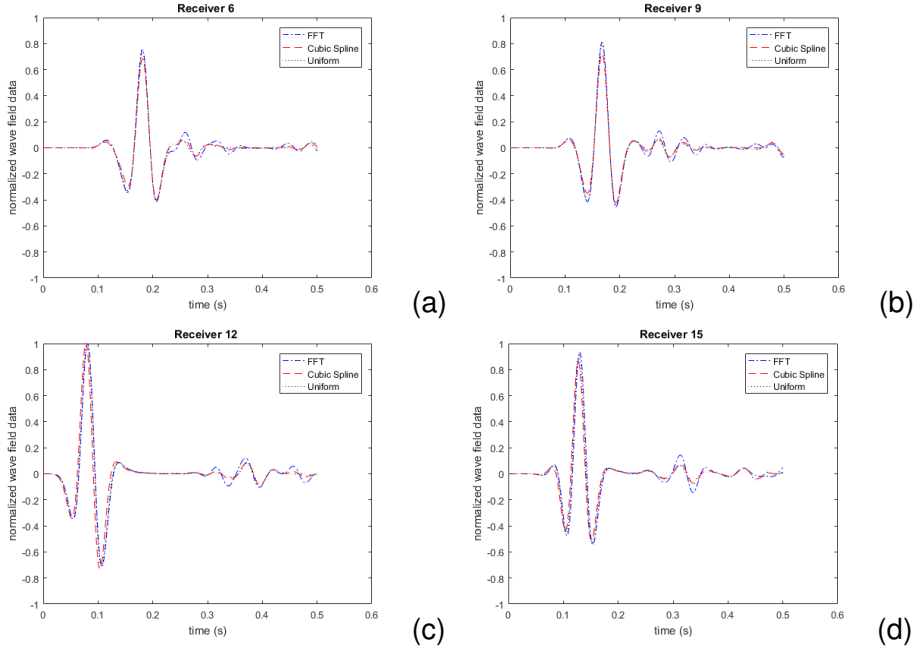

Figure 12: Comparison between wave fields generated by fast Fourier interpolation and cubic smoothing spline interpolation.